AGU PUBLICATIONS

JGR

Journal of Geophysical Research: Atmospheres

RESEARCH ARTICLE
10.1002/2015JD023425

Key Points:
- Atmospheric Hg at DAO is influenced by both anthropogenic and natural emissions
- Main emission source area for high-level Hg concentration is Yangtze River Delta
- Local meteorological conditions influence Hg input and diffusion rate

Supporting Information:
- Figures S1–S3, Table S1, and Text S1

Correspondence to:
X. Feng,
fengxinbin@vip.skleg.cn

Citation:
Yu, B., X. Wang, C.-J. Lin, X. Fu, H. Zhang, L. Shang, and X. Feng (2015), Characteristics and potential sources of atmospheric mercury at a subtropical near-coastal site in East China, *J. Geophys. Res. Atmos.*, *120*, 8563–8574, doi:10.1002/2015JD023425.

Received 24 MAR 2015
Accepted 3 AUG 2015
Accepted article online 6 AUG 2015
Published online 29 AUG 2015

Characteristics and potential sources of atmospheric mercury at a subtropical near-coastal site in East China

Ben Yu[1,2], Xun Wang[1,2], Che-Jen Lin[1,3,4], Xuewu Fu[1], Hui Zhang[1,2], Lihai Shang[1], and Xinbin Feng[1]

[1]State Key Laboratory of Environmental Geochemistry, Institute of Geochemistry, Chinese Academy of Sciences, Guiyang, China, [2]College of Earth Science, University of Chinese Academy of Sciences, Beijing, China, [3]Department of Civil and Environmental Engineering, Lamar University, Beaumont, Texas, USA, [4]College of Energy and Environment, South China University of Technology, Guangzhou, China

Abstract To evaluate the impact of regional mercury (Hg) emissions and understand possible source regions of atmospheric Hg in Eastern China, 2 year observation for speciated atmospheric Hg was conducted at the Dameishan Atmospheric Observatory, a mountain site near the east coast of China. The observed concentration of total gaseous Hg (TGM) was 3.3 ± 1.4 ng m^{-3}. During the sampling period, gaseous oxidized Hg and particulate bound Hg were 6.7 ± 4.3 pg m^{-3} and 180 ± 110 pg m^{-3} in winter and 5.9 ± 3.4 pg m^{-3} and 130 ± 100 pg m^{-3} in spring, respectively. The relatively high mean concentration of TGM was mainly caused by regional anthropogenic emissions and occasional long-range transport from domestic source regions. Seasonal variation in the TGM concentration was observed with lower values in the wet monsoon season (from May to September) and higher values in the dry monsoon season (from October to April). Backward trajectories and potential source contribution function analysis suggested that anthropogenic Hg emission from coal combustion in the Yangtze River Delta region was the most likely cause for the elevated TGM concentrations. Relatively clean air originating from the East China Sea was the most possible cause for the observed low TGM concentrations. Positive correlation between TGM concentration and air quality index suggests that emissions that influenced regional air quality contributed to the elevated TGM concentrations.

1. Introduction

Mercury (Hg) is a potent toxic air pollutant subject to long-range transport through global air circulation and causes contamination in regions remote from emission sources [*Schroeder and Munthe*, 1998]. The three major forms of atmospheric Hg are analytically defined as gaseous elemental Hg (GEM), gaseous oxidized Hg (GOM), and particulate bound Hg (PBM) [*Gustin and Jaffe*, 2010; *Schroeder and Munthe*, 1998]. GEM is mildly reactive in the troposphere, with a residence time of 0.5 to 2 years. GOM can be produced by both heterogeneous and homogeneous reactions [*Gustin et al.*, 2013] and readily removed from the lower troposphere [*Lindberg et al.*, 2007; *Schroeder and Munthe*, 1998]. PBM has a residence time of days to weeks. Total gaseous Hg (TGM) is defined as the sum of GEM and GOM concentrations. Hg can be emitted into the atmosphere from natural and anthropogenic sources [*Lindberg et al.*, 2007; *Schroeder and Munthe*, 1998]. Natural emissions, including the emission from geologic sources and the reemission of previously deposited Hg, make up approximately two thirds of global Hg emission [*Schroeder and Munthe*, 1998]. Human activities emit 1960 Mg of Hg into the atmosphere per year with Asia contributing >50% of the release (777 Mg yr^{-1} from East and Southeast Asia) [*Pirrone et al.*, 2010; *Selin et al.*, 2007; *United Nations Environment Programme*, 2013]. East China (including Shanghai, Anhui, Jiangsu, Zhejiang, Fujian, Jiangxi, and Shandong Provinces) is an important source region of atmospheric Hg in China, constituting approximately 20% of the total emissions [*Wu et al.*, 2006].

Long-term monitoring of speciated Hg in air facilitates understanding of the temporal trends, regional transport patterns, and source contributions of atmospheric Hg. Several monitoring networks have been established worldwide, including the Atmospheric Mercury Network, the Global Mercury Observation System, the Canadian Air and Precipitation Monitoring Network, and the European Monitoring and Evaluation Programme [*Ebinghaus et al.*, 2011; *Kellerhals et al.*, 2003; *Poissant et al.*, 2005; *Sigler et al.*, 2009; *Slemr et al.*, 2011; *Sommar et al.*, 2010; *Song et al.*, 2015; *Valente et al.*, 2007]. Observations of atmospheric Hg in China are relatively limited in terms of geographical coverage [*Feng et al.*, 2002, 2003, 2004; *Fu et al.*,

2010, 2012b; *Wang et al.*, 2007]. In particular, there are few long-term atmospheric Hg observations in the Yangtze River Delta region [*Wang et al.*, 2014; *Zhu et al.*, 2014]. This region is under the influence of subtropical monsoon climate. Long-term atmospheric Hg measurements in the region provide a unique opportunity to investigate the influences of the regional emissions and the seasonal monsoon on the characteristics of Hg in air.

In this study, we report the data from 2 year measurement of TGM and speciated atmospheric Hg during selected periods at the Dameishan Atmospheric Observatory (DAO) in the Yangtze River Delta region. Based on the TGM and meteorological data, cluster analysis of backward air trajectories and Potential Source Contribution Function (PSCF) analysis are performed to identify the potential source regions and transport pathways of atmospheric Hg. The effect of seasonal monsoon climate on the measured TGM concentrations is also discussed.

2. Experiment

2.1. Site Description

The measurement was carried out at the Dameishan Atmospheric Observatory, Chinese Academy of Sciences (121°33′E, 29°37′N, 550 m above sea level). The observatory is located at the summit of Mount Damei near the east coast of Zhejiang Province (~15 km from the coast). The monitoring station is situated in an open area (10 m × 10 m) surrounded by broadleaf deciduous forest. The meteorology at DAO is characterized by hot rainy summers and cold dry winters. The wind system is dominated by the West Pacific Subtropical High from May to September and East Asia Westerlies from October to April.

There is no point source of Hg emission within a radius of 10 km from DAO. The site is 22 km south of Ningbo, a major city in a megacity cluster located in the Yangtze River Delta extending from Shanghai. Atmospheric Hg emissions in Shanghai and Zhejiang Provinces were 10.5 Mg and 21.0 Mg in 2003 [*Wu et al.*, 2006]. The concentration of GEM at Shuangqiao farm in Jiaxing County (another observational site in the Yangtze River Delta, 140 km northwest of DAO) was 5.4 ± 4.1 ng m^{-3} as reported by a previous study [*Wang et al.*, 2007].

Meteorological data, including wind direction, wind speed, air temperature, daylight duration, and relative humidity (RH) at a weather station in Hengxi County (where DAO is located), were obtained from the China Meteorological Data Sharing Service System, China Meteorological Administration National Meteorological Information Center. The calculation of the daily meteorological data was based on the mean of the 6 h interval data (02:00, 08:00, 14:00, and 20:00, Beijing Time). The mean temperature and RH during the sampling period was 19.3°C and 75%, respectively.

2.2. Measurement of TGM, GOM, and PBM

TGM was measured every 5 min using a Tekran Model 2537B Hg vapor analyzer at 0.75 L min^{-1} sampling flow rate [*Fu et al.*, 2012a; *Lindberg et al.*, 2000; *Rutter et al.*, 2011; *Zhang et al.*, 2015]. This analyzer was housed in a laboratory with temperature controlled at 24–26°C. The sampling inlet was installed outdoors at 5.5 m above ground level (agl) and connected to the inlet of the 2537B using a thermally insulated Teflon tube (inner diameter: 5/32 inch; length: ~6 m). Two filters (47 mm Teflon membrane filter, pore size 0.2 μm) renewed weekly were installed: one at the air inlet and the other at sampling inlet of the Tekran 2537B. The air inlet filter was utilized to prevent particulate matter, droplets, and insects from entering the sampling line. A soda lime trap was connected prior to the filter holder at the inlet of the 2537B to remove reactive/acidic gases and water vapor in the sampled air. The 2537B was calibrated automatically using an internal standard every 23 h and manually by injecting standard Hg vapor from a permeation source (Tekran 2505) every 3 months. The analytical difference between the two parallel gold cartridges was controlled to be under 10%. The detect limit of the Tekran 2537B is 0.1 ng m^{-3}.

The measured Hg concentration is reported as TGM (GEM + GOM) since no sampling device for removing GOM was utilized. We recognize that GOM could be partially removed by the Teflon sampling tube [*Gustin et al.*, 2013]. However, the reported TGM concentration is representative because the GOM concentration at the site was $<$0.5% of TGM. The air residence time in the sampling tube is estimated to be ~6 s, which is short compared to the typical characteristic time of sorption/desorption, and therefore, the influence caused by the loss of GOM is insignificant. Based on the lab examination results of the sampling apparatus, the

sampling tube with the air inlet filter did not result in statistically different TGM concentration compared to direct air sampling using the Tekran 2537B.

GOM and PBM measurements were conducted in winter (December 14–19, 2012) and spring (March 13–19, 2013) using a methodology developed in our group [*Fu et al.*, 2012a; *Landis et al.*, 2002; *Zhang et al.*, 2015]. The sampling period (winter and spring) of GOM and PBM was selected to coincide with the period when anthropogenic Hg emission is higher with smaller influence from clean marine air. A quartz annular denuder (URG Corp., USA) was vertically installed outdoors with the inlet composed by a glass impactor plate to remove the coarse particles (greater than 2.5 μm in diameter) in ambient air. A downstream Teflon filter holder, in which a 47 mm diameter quartz fiber filter (GE Healthcare Life Sciences, air retention efficiency of greater than or equal to 99.95% of 0.3 μm size particulates) was placed at the outlet of the denuder to collect PBM in the ambient air. The denuder was coated with KCl for trapping GOM. Denuders and quartz fiber filters were pre-cleaned at 500°C and 850°C for 30 min. During the sampling period, the denuder was kept at 40–50°C by a temperature-controlled heating jacket to prevent condensation of water vapor. The sampling flow rate was maintained at 10 L min^{-1} by a vacuum pump (KNF Technology, Germany), and the sampled volume was recorded by a gas-volume meter (CHINT Instrument, China) downstream. The sampling duration was set to 4 h to collect a sufficient amount of GOM and PBM. After field sampling, the quartz fiber filter was transferred into a precleaned quartz tube (URG Corp., USA). Then both the quartz tube and the denuder were sealed using clean Teflon caps. To measure GOM and PBM by Tekran 2537B, thermal desorption of the Hg on the denuder or quartz filter were conducted at 500°C and 850°C for 15 min, respectively. The Hg-free carrier air was produced by the Tekran 1100 zero air generator.

The Hg concentration in the carrier gas through the nonheated quartz tube and denuder was measured as field blank before each analysis of GOM or PBM. Parallel denuders were deployed to sample continuously. The comparison and calibration of the parallel denuders were carefully conducted on site, and the deviation was controlled to be $<10\%$ ($n = 5$). The mean field blanks of denuder and filter were 0.22 ± 0.55 pg ($n = 53$) and 0.43 ± 0.65 pg ($n = 53$), respectively. The field sampling efficiency of the KCl-coated denuder can be influenced by RH and ozone concentration [*Gustin et al.*, 2013; *Huang et al.*, 2013; *Lyman et al.*, 2010; *McClure et al.*, 2014], and therefore, the reported GOM/PBM concentration should be regarded qualitatively.

2.3. Backward Trajectories and Potential Source Contribution Function Analysis

Three day backward air trajectories arriving at DAO at a height of 500 m agl were calculated to understand the transport pathways for TGM using the Hybrid Single-Particle Lagrangian Integrated Trajectory Model (HYSPLIT4) [*Draxler and Hess,* 1997, 1998; *Draxler et al.*, 1999]. The arrival height is below the typical mixing height (about 1 km agl) and therefore representative of sampling location. Hourly meteorological data were prepared using the Weather Research and Forecasting (WRF) model Version 3.4 with the Noah Land Surface Model, single-moment six-class microphysics scheme, Kain-Fritsch cumulus scheme, Dudhia radiation physics scheme, and Yonsei University (YSU) scheme for planetary boundary layer. The model domain is in Lambert Conformal projection covering the East Asian area, with 210×180 grid cells at 36 km spatial resolution. The center of model domain is 29.68°N, 121.62°E. The output of WRF was converted into HYSPLIT compatible format using a NOAA-Air Resources Laboratory utility program.

The endpoints of the backward trajectories were applied in Potential Source Contribution Function (PSCF) analysis [*Choi et al.*, 2008; *Fu et al.*, 2012a; *Kim et al.*, 2005]. The geophysical region centered by DAO (101° to 141°E, 9° to 49°N) was divided into 160,000 grid cells of 0.1×0.1 latitude and longitude. A weighing function W_{ij} was utilized to adjust the value of N_{ij} for small sample size [*Wang et al.*, 2009]. W_{ij} reduces the PSCF values when the total number of endpoints in a particular cell (N_{ij}) is less than 3 times the average value (N_{ave}) of the endpoints per cell.

$$W_{ij} = \begin{cases} 1.0 & N_{ij} \geq 3N_{ave} \\ 0.70 & 3N_{ave} > N_{ij} \geq 1.5N_{ave} \\ 0.40 & 1.5N_{ave} > N_{ij} \geq N_{ave} \\ 0.20 & N_{ave} > N_{ij} \end{cases} \quad (1)$$

In this study, the number of endpoints using in the PSCF analysis ranged from 64,343 to 66,629.

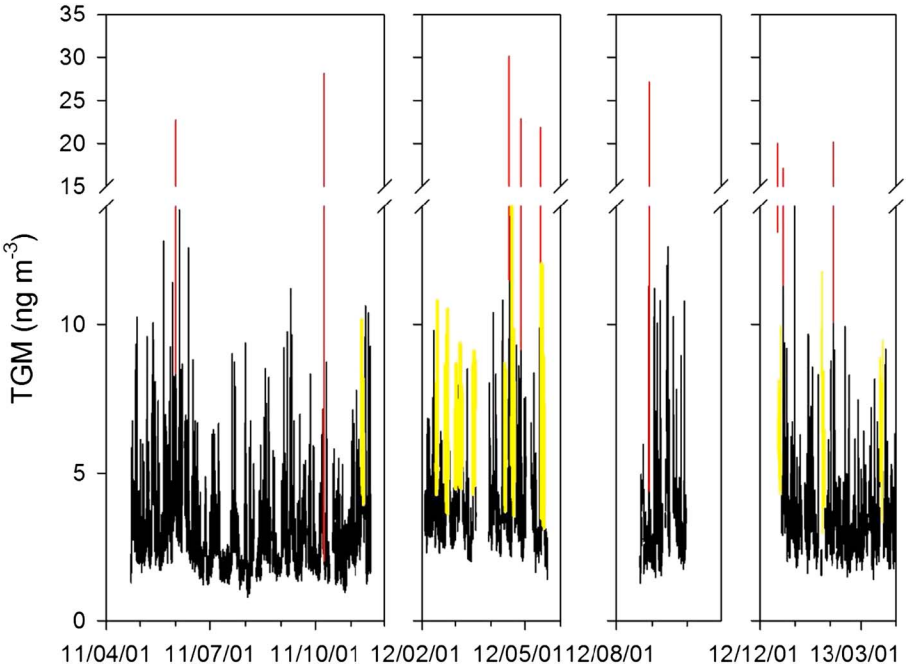

Figure 1. Time series of TGM concentrations in ambient air at DAO. The values in red show the nine transient high-TGM events. The values in yellow exhibit the pollution events.

3. Results and Discussion

3.1. Atmospheric Concentrations of TGM, GOM, and PBM

The time series of TGM concentration at DAO from 22 April 2011 to 21 April 2013, is shown in Figure 1. The TGM concentration was 3.3 ± 1.4 ng m^{-3}, higher than the concentrations observed at most remote sites in Europe and U.S. (<2 ng m^{-3}) [*Choi et al.*, 2008; *Engle et al.*, 2010; *Kock et al.*, 2005; *Sigler et al.*, 2009] and in SW and NW China (1.6–2.6 ng m^{-3}) [*Fu et al.*, 2010, 2012a, 2012b], but lower than the concentrations observed at urban sites in China (e.g., 4.9–8.3 ng m^{-3} in Beijing, 13.5 ± 7.1 ng m^{-3} in Guangzhou, 5.4 ± 4.1 ng m^{-3} in Yangtze River Delta, and 3.8 ± 1.3 ng m^{-3} in Ningbo) [*Wang et al.*, 2007; *Nguyen et al.*, 2011]. The elevated mean concentration suggests the influence from local and regional Hg emissions, with possible contributions from industrial processes (including power plants, steel plants, and cement plants) and domestic heating in industrial/urban areas in Eastern China.

Elevated atmospheric Hg concentrations measured using Tekran instruments have been reported in a number of Asian sites. For example, the mean Hg concentration observed in Seoul was 3.2 ± 2.1 ng m^{-3} [*Kim et al.*, 2009]. The Hg concentration at Hedo station, Okinawa, Japan, measured during the spring 2004 ranged from 1.4 ng m^{-3} to 4.7 ng m^{-3} [*Jaffe et al.*, 2005]. These sites are relatively close to the areas with large population and therefore subject to the influence of anthropogenic emissions. Much lower GEM (1.7 ± 0.6 ng m^{-3}) was observed at Lulin Atmospheric Background Station in Taiwan [*Sheu et al.*, 2010], due to the frequent influence of free troposphere air at the high-altitude background station. A comparison among the concentrations observed at these sites is summarized in the supporting information (Table S1).

Figure 2 shows the time series and statistics of GOM and PBM concentrations during the selected sampling periods. The GOM and PBM concentrations at DAO were 6.7 ± 4.3 pg m^{-3} and 180 ± 110 pg m^{-3} in winter and 5.9 ± 3.4 pg m^{-3} and 130 ± 100 pg m^{-3} in spring. The GOM/PBM concentrations in winter and in spring were not significantly different from each other (t test). Using the same speciation measurements, the concentrations of GOM at DAO are similar to those observed elsewhere, while the concentrations of PBM at DAO are much higher than the concentrations measured at remote sites and urban/suburban areas [*Choi et al.*, 2008; *Engle et al.*, 2010; *Fu et al.*, 2012a; *Sigler et al.*, 2009]. The GOM and PBM concentrations are possibly influenced by local anthropogenic Hg sources during the sampling

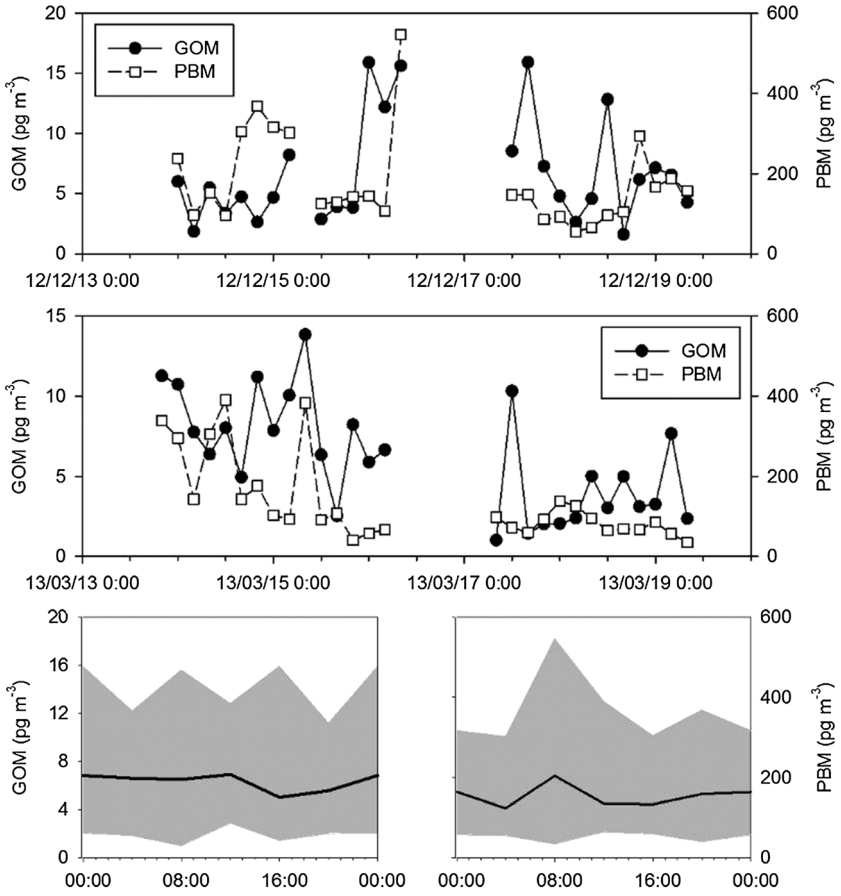

Figure 2. Time series plot and temporal trend of GOM and PBM concentrations at DAO during selected periods (UTC + 8:00). The concentrations in the time series plots (upper two panels) are recorded at the end of sampling duration. Data statistics are illustrated in ranges (gray area) and mean (straight line).

period. The RH (average 75% during sampling period) at DAO was high, which could lead to substantial GOM removal from the ambient air [*Laurier et al.*, 2003; *Sheu and Mason*, 2001]. The sea salt aerosol from marine-sourced air masses could absorb GOM [*Holmes et al.*, 2009] and lower its concentration, and therefore, the observed GOM concentration was relatively low despite the influence of anthropogenic emissions at DAO. Elevated PBM concentration implies the influence from anthropogenic emission of PM. Higher concentrations of PBM were observed after sunrise, which might be from the increase of human activities during the daytime. A longer sampling duration is necessary to better understand the temporal trend of GOM and PBM at the site.

3.2. Wind Dependence of TGM

Annual and seasonal wind roses are shown in the supporting information (Figure S1). Prevailing winds in summer were from south and east due to the East Asia Monsoon in contrast to the prevailing winds from north in winter. The northerly wind moving over the Yangtze River Delta in winter and spring frequently carried the regional emissions to DAO (mean TGM concentration: 3.4–4.3 ng m^{-3} in winter and 3.4–4.8 ng m^{-3} in spring). The emission sources included coal-fired power plants, cement plants, steel plants, waste incineration plants, and boilers for domestic heating and solid waste [*Streets et al.*, 2005]. The northeasterly wind that carried high TGM from the source region weakened in autumn, leading to much lower TGM concentrations. Southerly wind from the East China Sea typically had relatively low TGM concentrations (mean TGM concentration ranged from 2.3 to 3.7 ng m^{-3} during the entire monitoring period). WNW, NW, NNW, ENE, and SSW winds appeared to be associated with higher Hg concentration during the entire monitoring period. WNW, NW, and NNW winds pointed to the direction where the city cluster in the Yangtze River Delta region is located. ENE winds pointed to the neighboring residential areas

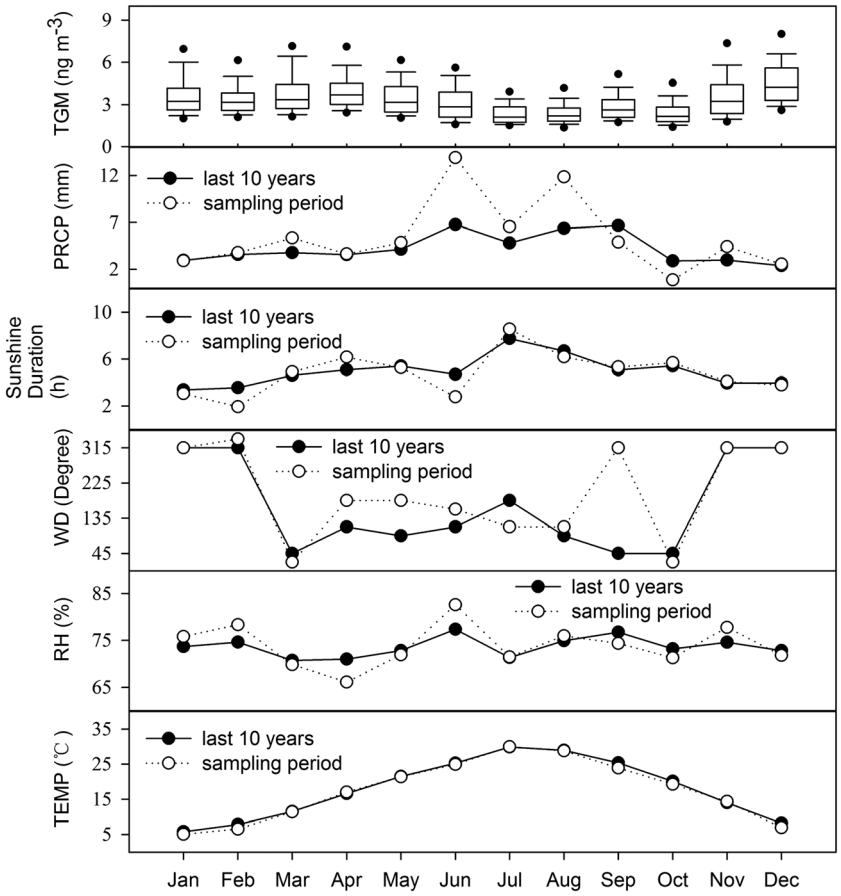

Figure 3. Monthly variation of meteorological data, including precipitation (PRCP), sunshine duration, wind direction (WD), relative humidity (RH) and temperature (TEMP), and the associated TGM concentration. (first panel) The box plot shows the 25th, 50th, and 75th percentiles. The lower and upper whiskers represent the 10th and 90th percentiles. The dots outside the box-and-whisker plot represent the 5th and 95th percentiles.

of Zhoushan City and Xiangshan County, while SSW pointed to the industrial/urban areas located at the eastern coastline of China.

Figure S2 shows the relationship between the wind direction and TGM concentration in the wet and dry seasons. The days influenced by sea breezes in the wet monsoon had relatively higher precipitation (6.9 ± 16.6 mm), RH (74.8 ± 8.6%), and temperature (26.6 ± 3.5°C) but lower TGM concentration (2.6 ± 0.9 ng m^{-3}). The days influenced by terrestrial winds in the dry monsoon exhibited different meteorological characteristics and higher TGM concentration (precipitation 4.0 ± 6.9 mm, RH 74.2 ± 12.9%, temperature 10.3 ± 6.2°C, and TGM concentration 3.7 ± 1.3 ng m^{-3}).

3.3. Monthly, Seasonal, and Diurnal Variations

Monthly variation of TGM concentrations and meteorological data during the sampling period and in the last 10 years before sampling (2000–2010) is illustrated in Figure 3. During the warm months (from April to August), the wind direction was either south or east from the East China Sea. North and west were the dominant wind directions from September to February. The lowest monthly mean occurred in July (2.4 ng m^{-3}). The highest monthly mean occurred in December (4.7 ng m^{-3}). The higher TGM concentration in the cold season and lower concentration in the warm season are consistent with previous results at sites influenced by local anthropogenic Hg emissions in China [*Feng et al.*, 2002, 2003, 2004; *Fu et al.*, 2012c; *Wang et al.*, 2007]. This is in contrast to TGM concentrations observed at sites influenced by long transport [*Fu et al.*, 2012a], during which dilution and mixing by air masses can influence the dispersion of Hg plumes.

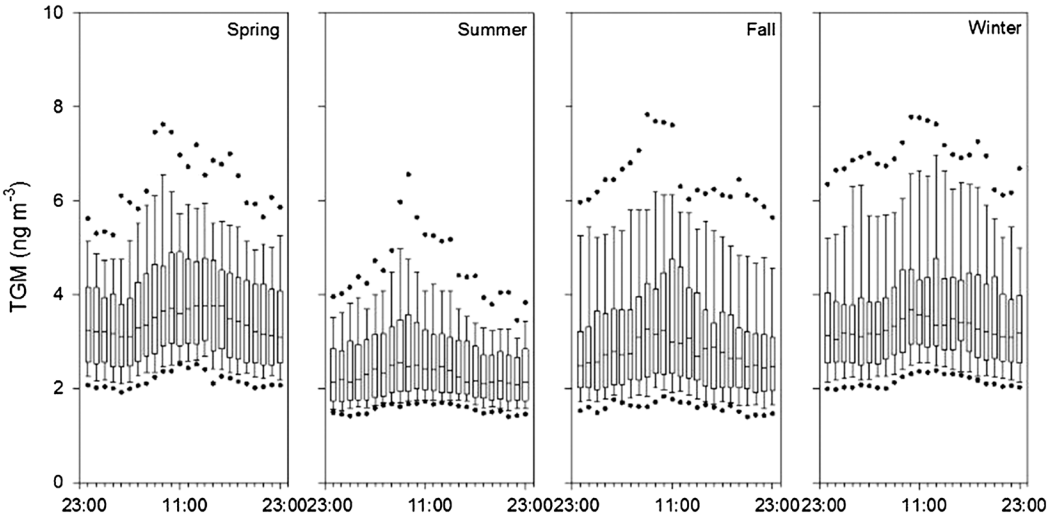

Figure 4. Diurnal variation of TGM in different seasons at DAO.

The seasonal diurnal variation of TGM concentration is shown in Figure 4. The highest mean TGM concentration was 3.7 ng m^{-3} in winter, and the lowest value was 2.6 ng m^{-3} in summer. There are several possible reasons for the observed trends. Summer winds mainly came from the sea and carried air masses with low TGM concentration that diluted the TGM concentration at DAO. In addition, enhanced photochemical activity in summer could accelerate the removal of TGM. In winter, the shallower planetary boundary layer could capture the TGM in the mixing layer [*Mao et al.*, 2008]. The regional Hg emissions were larger in winter because of increased coal combustion. This seasonal pattern of TGM concentration (~1.5X higher concentration in winter compared to that in summer) was similar to that of organic carbon (OC) and $PM_{2.5}$ in the region [*Feng et al.*, 2009].

As shown in Figure 4, a higher concentration occurred in the morning for all seasons. Such a diurnal trend is similar to the morning pollutant accumulation in urban areas due to increased human activities during daytime [*Fu et al.*, 2008; *Wang et al.*, 2007]. Another possible reason is the diurnal wind pattern. Atmospheric Hg released from industrial areas adjacent to DAO was enriched during the night due to the shallow nocturnal boundary layer [*Feng et al.*, 2004; *Fu et al.*, 2012b; *Lee et al.*, 1998]. After sunrise, the plume was uplifted to the monitoring site. A third possible factor is the reemission of deposited Hg from the forest floor due to the elevated soil temperature after sunrise [*Gustin et al.*, 2004; *Peterson et al.*, 2009]. The reemission could contribute to the peak concentration above the canopy in the morning. The concentration peaks were much broader in winter and spring possibly because anthropogenic emissions were more active during the day due to residential heating.

3.4. Transient High-TGM Events

Nine transient high-TGM events were identified in the 2 year monitoring period (Figure 1 and Table 1). Such concentration spikes (≥15.0 ng m^{-3} and up to 30.1 ng m^{-3}) occurred in short durations (<30 min) and were

Table 1. Characteristics of TGM and Wind During Nine Transient High-TGM Events

Events	Start Time (UTC + 8:00)	End Time (UTC + 8:00)	Mean TGM (ng m^{-3})	Peak (ng m^{-3})	Wind Direction	Wind Speed (m s^{-1})
1	2011/6/1 3:35	2011/6/1 3:55	16.08	22.72	SSE	5.28
2	2011/10/8 12:55	2011/10/8 13:05	10.80	28.11	NE	12.18
3	2012/4/17 4:30	2012/4/17 5:00	21.84	30.09	NE	8.03
4	2012/4/27 8:40	2012/4/27 9:15	16.47	22.84	WSW	6.73
5	2012/5/14 20:30	2012/5/14 20:50	15.59	21.84	NW	8.3
6	2012/8/29 9:15	2012/8/29 9:35	17.14	27.16	E	6.32
7	2012/12/16 12:50	2012/12/16 13:40	17.70	19.97	ESE	8.64
8	2012/12/21 9:05	2012/12/21 9:20	14.59	17.11	SE	16.33
9	2013/2/4 11:45	2013/2/4 12:05	15.06	20.16	SSW	7.86

Table 2. Period of Pollution Events and the Associated TGM Concentration

Events	Start Time (UTC + 8:00)	End Time (UTC + 8:00)	Duration (h)	Mean TGM (ng m^{-3})
1	2011/11/11 2:00	2011/11/12 14:00	36	5.51 ± 0.69
2	2012/2/13 6:00	2012/2/14 19:00	37	6.36 ± 1.20
3	2012/2/21 13:00	2012/2/23 18:00	53	5.73 ± 1.82
4	2012/3/1 7:00	2012/3/2 16:00	33	6.23 ± 0.70
5	2012/3/4 14:00	2012/3/7 7:00	65	6.48 ± 0.85
6	2012/3/16 11:00	2012/3/18 13:00	50	6.92 ± 1.11
7	2012/4/13 5:00	2012/4/14 15:00	34	5.43 ± 0.99
8	2012/4/19 11:00	2012/4/21 13:00	50	6.42 ± 1.72
9	2012/5/15 10:00	2012/5/17 18:00	56	5.37 ± 1.18
10	2012/12/17 0:00	2012/12/19 18:00	66	5.91 ± 0.67
11	2013/1/24 16:00	2013/1/27 12:00	68	5.71 ± 1.71
12	2013/3/17 22:00	2013/3/20 11:00	61	6.20 ± 1.28

commonly observed at urban sites [*Feng et al.*, 2004; *Friedli et al.*, 2011; *Song et al.*, 2009]. These events were associated with different wind directions and speeds, suggesting different emission sources. The characteristics of these transient high-TGM events were different from the diluted Hg plume after long-range transport. These spikes were most likely caused by short-term Hg emissions (e.g., small-scaled biomass burning) near DAO.

3.5. Pollution Events

There is no geogenic Hg emission source near DAO. Therefore, the observed temporal trend and wind dependence of TGM suggest anthropogenic influence and atmospheric transport to the monitoring site. To understand the relationship between the elevated TGM concentration and wind direction/speed, 12 pollution events were identified using the following criteria: (a) the duration of elevated (defined as >90th percentile, 5.1 ng m^{-3}) hourly TGM concentration lasted for >24 h and (b) the period between the elevated

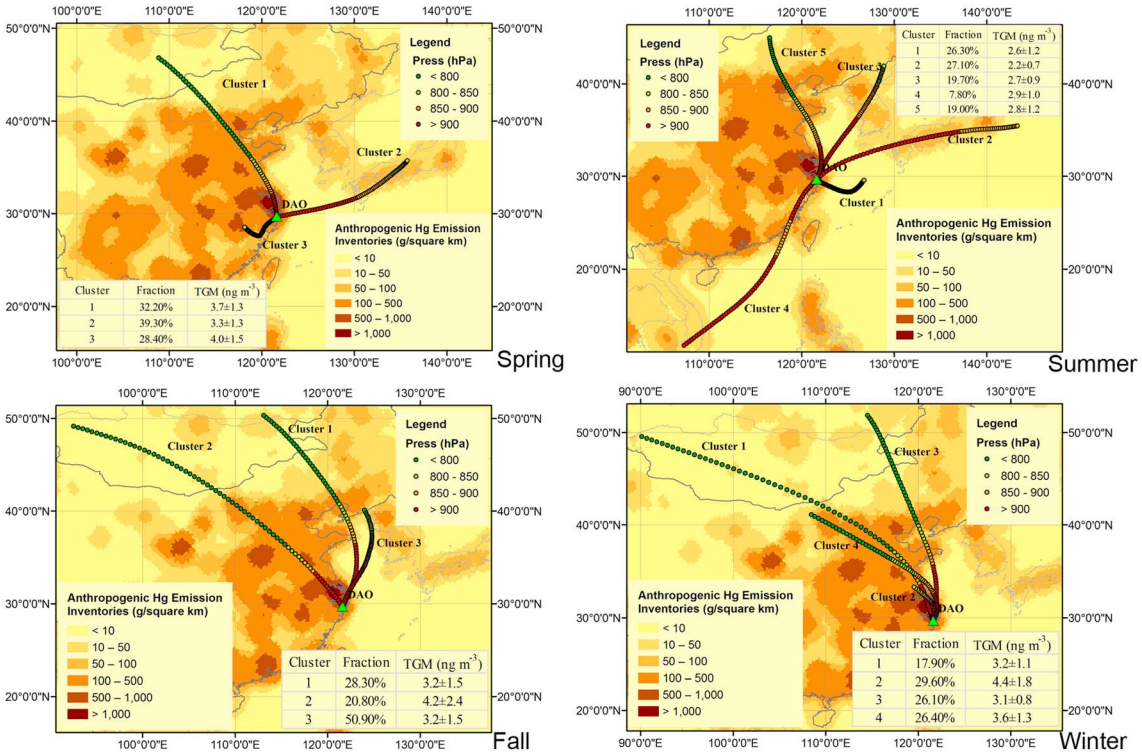

Figure 5. Clusters of the 3 day backward trajectories in (upper-left panel) spring, (upper-right panel) summer, (lower-left panel) autumn, and (lower-right panel) winter. Anthropogenic Hg emission inventories are illustrated based on Arctic Monitoring and Assessment Programme (AMAP) data. The height of the endpoints in each trajectory cluster is also illustrated.

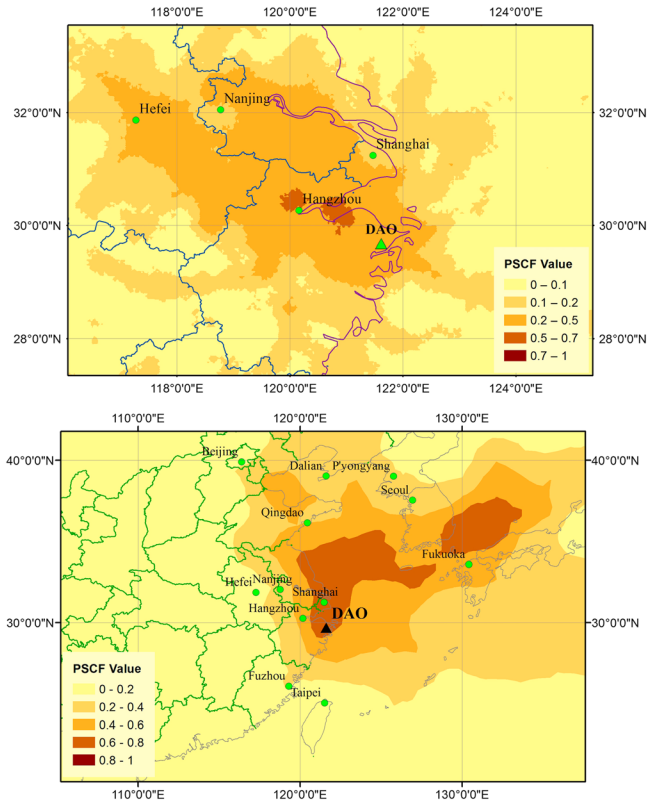

Figure 6. The source areas associated with (upper panel) high and (lower panel) low TGM concentrations observed at DAO.

TGM concentrations (i.e., the duration with the hourly TGM concentration $<5.1\,ng\,m^{-3}$) was shorter than 12 h. These 12 pollution events are shown in Figure 1 and listed in Table 2.

All pollution events occurred during dry season (January–May and November–December) when the meteorological conditions were dominated by terrestrial winds. As illustrated in Figure S3, air masses with elevated TGM concentration in most of the pollution events were from the NW, SW, and NE directions where the industrial and urban areas around DAO are located. The air masses from the SE direction, originating from the East China Sea, had lower TGM concentration (Events 3, 7, and 8). These patterns suggest that local-regional anthropogenic sources were the primary contributors to elevated TGM concentrations. Negative correlation between TGM concentration and wind speed was found in most pollution events. Higher wind speeds typically led to a greater air dilution, which resulted in the negative correlation. Positive correlations between wind speed and TGM concentrations persisted for several hours during Events 3, 9, 10, and 11. These events mostly occurred during the night and were possibly caused by a shallow nocturnal boundary layer that trapped the Hg emission from regional sources.

3.6. Transport Pathways of TGM

Concentrations of TGM are closely related to sources and transport pathways. Cluster analysis of the 3 day backward trajectories was performed using a hierarchical Ward's method [*Wang et al.*, 2009] to understand the transport pathways (Figure 5). To illustrate the influences of anthropogenic Hg emissions, the emission inventory is also shown in each panel of Figure 5. In spring, three clusters are formed. Cluster 1 originated from central Mongolia and transported across the North China Plain with heavy Hg emissions. Cluster 2 originated from southern Japan and transported over the East China Sea. Cluster 3 originated from the junction of Jiangxi, Zhejiang, and Fujian Provinces and moved to DAO from southwest with the highest mean TGM concentration of $4.0 \pm 1.5\,ng\,m^{-3}$. In summer, clusters 1–3 originated from the East China Sea, Japan, and west side of the Sea of Japan. Cluster 4 originated from Southeast Asia and transported over the South China Sea through the southeast coast of China with highest TGM concentration of $2.9 \pm 1.0\,ng\,m^{-3}$. Cluster 5 originated from Inner Mongolia Province and passed through the North China Plain. In fall, three clusters came from the north. Cluster 2 had the highest TGM concentration at $4.2 \pm 2.4\,ng\,m^{-3}$. All four clusters originated within the mainland China in winter. Cluster 2, much shorter than the others, originated from central part of Jiangsu Province and passed over the Yangtze River Delta with the highest value of $4.4 \pm 1.8\,ng\,m^{-3}$. In each season, clusters originating from marine areas or transport from the marine area (including cluster 2 in spring; clusters 1–3 and 5 in summer; cluster 1 and 3 in fall; and cluster 3 in winter, with TGM concentrations ranging from $2.2 \pm 0.7\,ng\,m^{-3}$ to $3.3 \pm 1.3\,ng\,m^{-3}$) had lower TGM concentration compared to those clusters passing over terrestrial regions (with TGM concentrations ranging from $2.9 \pm 1.0\,ng\,m^{-3}$ to $4.4 \pm 1.8\,ng\,m^{-3}$). Clusters

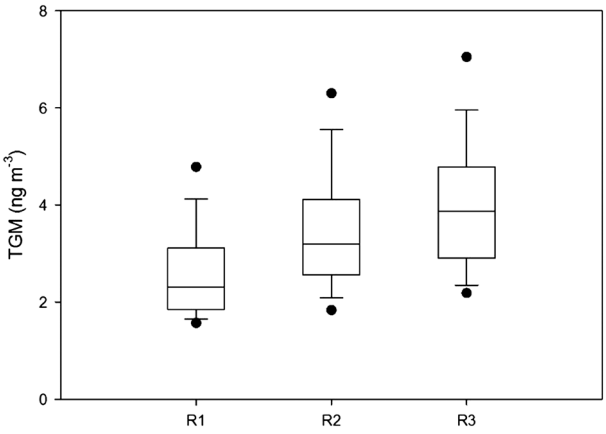

Figure 7. Hourly mean TGM concentration associated with various AQI values. Rank 1 (R1) represents the AQI values of <50. Rank 2 (R2) represents the AQI values between 50 and 100. Rank 3 (R3) represents the AQI values of >100.

transported across industrial areas including the Yangtze River Delta region and the coastal areas of southeast China had elevated TGM concentrations, suggesting influences from anthropogenic Hg emissions in industrial/urban areas.

3.7. Potential Source Regions for High- and Low-Concentration Hg Emissions

Trajectory endpoints associated with high TGM concentrations (>90th percentile, 5.1 ng m^{-3}) were selected to create the PSCF map. Results shown in Figure 6 suggest that industrial and urban areas in the Yangtze River Delta and the neighboring region of Anhui, Jiangsu, and Zhejiang Provinces were important source areas, consistent with the Arctic Monitoring and Assessment Programme (AMAP) inventory data. The observed TGM was mostly from regional anthropogenic emissions northwest of DAO. Trajectories associated with low TGM concentrations (<10th percentile, 1.9 ng m^{-3}) were also selected to create the PSCF map (Figure 6). The East China Sea, the Bohai Sea, and the East Japan Sea were identified as the high-PSCF regions, suggesting that low TGM at DAO was mostly caused by the transport from marine areas. These results show that the TGM at DAO was influenced by both anthropogenic emissions inland and transport of clean air from the ocean, subject to the transition of seasonal subtropical monsoons.

3.8. Relationship Between Air Quality Index and TGM Concentration

Regional anthropogenic Hg emissions significantly contributed to the high TGM values observed at DAO. The air quality index (AQI, see detailed description in Text S1), released by the Chinese MEP with PM_{10}/SO_2 as the primary pollutants during the sampling period, reflected the local-regional air pollution level. An attempt was made to relate the regional AQI to the observed TGM concentrations. The hourly AQI showed positive correlation with the hourly concentrations of SO_2 and PM_{10} released from coal combustion in China [*Streets and Waldhoff*, 2000; *Ye et al.*, 2003]. The hourly mean TGM concentrations were plotted against three AQI ranks in Figure 7. R3 (AQI > 100) was associated with the highest concentration of TGM (4.1 ± 1.1 ng m^{-3}) while R1 (AQI < 50) was associated with the lowest one (2.8 ± 1.0 ng m^{-3}). This implies that the emissions from local coal combustion could have an important impact on the observed TGM concentration.

4. Conclusions

Continuous monitoring of TGM concentration and short-term measurements of GOM and PBM were conducted at DAO, an observatory station located at the edge of the southeast coastal area adjacent to the Yangtze River Delta region. The concentration of TGM at DAO was 3.3 ± 1.4 ng m^{-3}. The concentrations of GOM and PBM during the selected sampling period were 6.7 ± 4.3 pg m^{-3} and 180 ± 110 pg m^{-3} in winter and 5.9 ± 3.4 pg m^{-3} and 130 ± 100 pg m^{-3} in spring, respectively. TGM concentration at DAO was much higher than the observed concentrations at remote sites in North America and Europe but lower than those observed at urban sites in China. The seasonal, monthly, and diurnal variations of TGM concentration were similar to those of OC and $PM_{2.5}$, indicating the strong impact of regional anthropogenic emissions in the Yangtze River Delta region. The correlation between hourly TGM concentration and wind suggests that both local/regional anthropogenic emissions and meteorological conditions influenced the TGM concentration during pollution events. Backward air trajectories and PSCF analysis identified the Yangtze River Delta as the most important source region for the observed TGM. The transport of marine air from the East China Sea occasionally diluted the TGM concentration at DAO. Sea breezes brought lower TGM concentration during the wet monsoon, as compared to the elevated TGM concentration associated with terrestrial winds. The correlation between TGM concentration and the local AQI indicated that coal combustion had an important impact on the observed TGM concentration at DAO.

Acknowledgments
This work was supported by National "973" Program (2013CB430003) and Natural Science Foundation of China (41173024 and 41273145). We also thank Dameishan Atmosphere Observatory and Guangzhou Institute of Geochemistry, Chinese Academy of Sciences for field sampling assistance. Data can be obtained from Xinbin Feng (fengxinbin@vip.skleg.cn).

References

Choi, H. D., T. M. Holsen, and P. K. Hopke (2008), Atmospheric mercury (Hg) in the Adirondacks: concentrations and sources, *Environ. Sci. Technol.*, *42*(15), 5644–5653, doi:10.1021/es7028137.

Draxler, R. R., and G. Hess (1997), Description of the HYSPLIT4 modeling system, *NOAA Tech. Memo.* ERL ARL-224. NOAA Air Resources Laboratory, Silver Spring, Md., 24 pp.

Draxler, R. R., and G. Hess (1998), An overview of the HYSPLIT_4 modelling system for trajectories, *Aust. Meteorol. Mag.*, *47*(4), 295–308.

Draxler, R. R., B. Stunder, G. Rolph, and A. Taylor (1999), HYSPLIT4 user's guide, *NOAA Tech. Memo.* ERL ARL-230, NOAA Air Resources Laboratory, Silver Spring, Md.

Ebinghaus, R., S. G. Jennings, H. H. Kock, R. G. Derwent, A. J. Manning, and T. G. Spain (2011), Decreasing trends in total gaseous mercury observations in baseline air at Mace Head, Ireland from 1996 to 2009, *Atmos. Environ.*, *45*(20), 3475–3480, doi:10.1016/j.atmosenv.2011.01.033.

Engle, M. A., M. T. Tate, D. P. Krabbenhoft, J. J. Schauer, A. Kolker, J. B. Shanley, and M. H. Bothner (2010), Comparison of atmospheric mercury speciation and deposition at nine sites across central and eastern North America, *J. Geophys. Res.*, *115*, D18306, doi:10.1029/2010JD014064.

Feng, X. B., J. Sommar, O. Lindqvist, and Y. T. Hong (2002), Occurrence, emissions and deposition of mercury during coal combustion in the Province Guizhou, China, *Water Air Soil Pollut.*, *139*(1–4), 311–324, doi:10.1023/A:1015846605651.

Feng, X. B., S. L. Tang, L. H. Shang, H. Y. Yan, J. Sommar, and O. Lindqvist (2003), Total gaseous mercury in the atmosphere of Guiyang, PR China, *Sci. Total Environ.*, *304*(1–3), 61–72, doi:10.1016/S0048-9697(02)00557-0.

Feng, X. B., L. H. Shang, S. F. Wang, S. L. Tang, and W. Zheng (2004), Temporal variation of total gaseous mercury in the air of Guiyang, China, *J. Geophys. Res.*, *109*, D03303, doi:10.1029/2003JD004159.

Feng, Y., Y. Chen, H. Guo, G. Zhi, S. Xiong, J. Li, G. Sheng, and J. Fu (2009), Characteristics of organic and elemental carbon in PM 2.5 samples in Shanghai, China, *Atmos. Res.*, *92*(4), 434–442, doi:10.1016/j.atmosres.2009.01.003.

Friedli, H. R., A. F. Arellano, F. Geng, C. Cai, and L. Pan (2011), Measurements of atmospheric mercury in Shanghai during September 2009, *Atmos. Chem. Phys.*, *11*(8), 3781–3788, doi:10.5194/acp-11-3781-2011.

Fu, X. W., X. B. Feng, and S. F. Wang (2008), Exchange fluxes of Hg between surfaces and atmosphere in the eastern flank of Mount Gongga, Sichuan Province, southwestern China, *J. Geophys. Res.*, *113*, D20306, doi:10.1029/2008JD009814.

Fu, X. W., X. Feng, Z. Q. Dong, R. S. Yin, J. X. Wang, Z. R. Yang, and H. Zhang (2010), Atmospheric gaseous elemental mercury (GEM) concentrations and mercury depositions at a high-altitude mountain peak in south China, *Atmos. Chem. Phys.*, *10*(5), 2425–2437, doi:10.5194/acp-10-2425-2010.

Fu, X. W., X. Feng, P. Liang, H. Deliger, J. J. Zhang, and P. Liu (2012a), Temporal trend and sources of speciated atmospheric mercury at Waliguan GAW station, Northwestern China, *Atmos. Chem. Phys.*, *12*(4), 1951–1964, doi:10.5194/acp-12-1951-2012.

Fu, X. W., X. Feng, L. H. Shang, S. F. Wang, and H. Zhang (2012b), Two years of measurements of atmospheric total gaseous mercury (TGM) at a remote site in Mt. Changbai area, Northeastern China, *Atmos. Chem. Phys.*, *12*(9), 4215–4226, doi:10.5194/acp-12-4215-2012.

Fu, X. W., X. B. Feng, J. Sommar, and S. F. Wang (2012c), A review of studies on atmospheric mercury in China, *Sci. Total Environ.*, *421–422*, 73–81, doi:10.1016/j.scitotenv.2011.09.089.

Gustin, M. S., and D. A. Jaffe (2010), Reducing the uncertainty in measurement and understanding of mercury in the atmosphere, *Environ. Sci. Technol.*, *44*(7), 2222–2227, doi:10.1021/es902736k.

Gustin, M. S., J. A. Ericksen, D. E. Schorran, D. W. Johnson, S. E. Lindberg, and J. S. Coleman (2004), Application of controlled mesocosms for understanding mercury air-soil-plant exchange, *Environ. Sci. Technol.*, *38*(22), 6044–6050, doi:10.1021/es0487933.

Gustin, M. S., et al. (2013), Do we understand what the mercury speciation instruments are actually measuring? Results of RAMIX, *Environ. Sci. Technol.*, *47*(13), 7295–7306, doi:10.1021/es3039104.

Holmes, C. D., D. J. Jacob, R. P. Mason, and D. A. Jaffe (2009), Sources and deposition of reactive gaseous mercury in the marine atmosphere, *Atmos. Environ.*, *43*(14), 2278–2285, doi:10.1016/j.atmosenv.2009.01.051.

Huang, J. Y., M. B. Miller, P. Weiss-Penzias, and M. S. Gustin (2013), Comparison of gaseous oxidized Hg measured by KCl-coated denuders, and nylon and cation exchange membranes, *Environ. Sci. Technol.*, *47*(13), 7307–7316, doi:10.1021/es4012349.

Jaffe, D. A., E. Prestbo, P. Swartzendruber, P. Weiss-Penzias, S. Kato, A. Takami, S. Hatakeyama, and Y. Kajii (2005), Export of atmospheric mercury from Asia, *Atmos. Environ.*, *39*(17), 3029–3038, doi:10.1016/j.atmosenv.2005.01.030.

Kellerhals, M., et al. (2003), Temporal and spatial variability of total gaseous mercury in Canada: Results from the Canadian Atmospheric Mercury Measurement Network (CAMNet), *Atmos. Environ.*, *37*(7), 1003–1011, doi:10.1016/S1352-2310(02)00917-2.

Kim, E., P. K. Hopke, D. M. Kenski, and M. Koerber (2005), Sources of fine particles in a rural midwestern US area, *Environ. Sci. Technol.*, *39*(13), 4953–4960, doi:10.1021/Es0490774.

Kim, S. H., Y. J. Han, T. M. Holsen, and S. M. Yi (2009), Characteristics of atmospheric speciated mercury concentrations (TGM, Hg(II) and Hg(p)) in Seoul, Korea, *Atmos. Environ.*, *43*(20), 3267–3274, doi:10.1016/j.atmosenv.2009.02.038.

Kock, H. H., E. Bieber, R. Ebinghaus, T. G. Spain, and B. Thees (2005), Comparison of long-term trends and seasonal variations of atmospheric mercury concentrations at the two European coastal monitoring stations Mace Head, Ireland, and Zingst, Germany, *Atmos. Environ.*, *39*(39), 7549–7556, doi:10.1016/j.atmosenv.2005.02.059.

Landis, M. S., R. K. Stevens, F. Schaedlich, and E. M. Prestbo (2002), Development and characterization of an annular denuder methodology for the measurement of divalent inorganic reactive gaseous mercury in ambient air, *Environ. Sci. Technol.*, *36*(13), 3000–3009, doi:10.1021/es015887t.

Laurier, F. J., R. P. Mason, L. Whalin, and S. Kato (2003), Reactive gaseous mercury formation in the North Pacific Ocean's marine boundary layer: A potential role of halogen chemistry, *J. Geophys. Res.*, *108*(D17), 4529, doi:10.1029/2003JD003625.

Lee, D. S., G. J. Dollard, and S. Pepler (1998), Gas-phase mercury in the atmosphere of the United Kingdom, *Atmos. Environ.*, *32*(5), 855–864, doi:10.1016/S1352-2310(97)00316-6.

Lindberg, S. E., A. F. Vette, C. Miles, and F. Schaedlich (2000), Mercury speciation in natural waters: Measurement of dissolved gaseous mercury with a field analyzer, *Biogeochemistry*, *48*(2), 237–259, doi:10.1023/A:1006228612872.

Lindberg, S. E., R. Bullock, R. Ebinghaus, D. Engstrom, X. Feng, W. Fitzgerald, N. Pirrone, E. Prestbo, C. Seigneur, and M. Panel on Source Attribution of Atmospheric (2007), A synthesis of progress and uncertainties in attributing the sources of mercury in deposition, *Ambio*, *36*(1), 19–32, doi:10.1579/0044-7447(2007)36[19:ASOPAU]2.0.CO;2.

Lyman, S. N., D. A. Jaffe, and M. S. Gustin (2010), Release of mercury halides from KCl denuders in the presence of ozone, *Atmos. Chem. Phys.*, *10*(17), 8197–8204, doi:10.5194/acp-10-8197-2010.

Mao, H., R. W. Talbot, J. M. Sigler, B. C. Sive, and J. D. Hegarty (2008), Seasonal and diurnal variations of Hg° over New England, *Atmos. Chem. Phys.*, *8*(5), 1403–1421, doi:10.5194/acp-8-1403-2008.

McClure, C. D., D. A. Jaffe, and E. S. Edgerton (2014), Evaluation of the KCl denuder method for gaseous oxidized mercury using HgBr2 at an in-service AMNet site, *Environ. Sci. Technol.*, *48*(19), 11,437–11,444, doi:10.1021/es502545k.

Nguyen, D. L., J. Y. Kim, S. G. Shim, and X. S. Zhang (2011), Ground and shipboard measurements of atmospheric gaseous elemental mercury over the Yellow Sea region during 2007–2008, *Atmos. Environ.*, *45*(1), 253–260, doi:10.1016/j.atmosenv.2010.07.021.

Peterson, C., M. Gustin, and S. Lyman (2009), Atmospheric mercury concentrations and speciation measured from 2004 to 2007 in Reno, Nevada, USA, *Atmos. Environ.*, *43*(30), 4646–4654, doi:10.1016/j.atmosenv.2009.04.053.

Pirrone, N., et al. (2010), Global mercury emissions to the atmosphere from anthropogenic and natural sources, *Atmos. Chem. Phys.*, *10*(13), 5951–5964, doi:10.5194/acp-10-5951-2010.

Poissant, L., M. Pilote, C. Beauvais, P. Constant, and H. Zhang (2005), A year of continuous measurements of three atmospheric mercury species (GEM, RGM and Hg) in southern Québec, Canada, *Atmos. Environ.*, *39*(7), 1275–1287, doi:10.1016/j.atmosenv.2004.11.007.

Rutter, A. P., J. J. Schauer, M. M. Shafer, J. E. Creswell, M. R. Olson, M. Robinson, R. M. Collins, A. M. Parman, T. L. Katzman, and J. L. Mallek (2011), Dry deposition of gaseous elemental mercury to plants and soils using mercury stable isotopes in a controlled environment, *Atmos. Environ.*, *45*(4), 848–855, doi:10.1016/j.atmosenv.2010.11.025.

Schroeder, W. H., and J. Munthe (1998), Atmospheric mercury—An overview, *Atmos. Environ.*, *32*(5), 809–822, doi:10.1016/S1352-2310(97)00293-8.

Selin, N. E., D. J. Jacob, R. J. Park, R. M. Yantosca, S. Strode, L. Jaegle, and D. Jaffe (2007), Chemical cycling and deposition of atmospheric mercury: Global constraints from observations, *J. Geophys. Res.*, *112*, D02308, doi:10.1029/2006JD007450.

Sheu, G. R., N. H. Lin, J. L. Wang, C. T. Lee, C. F. O. Yang, and S. H. Wang (2010), Temporal distribution and potential sources of atmospheric mercury measured at a high-elevation background station in Taiwan, *Atmos. Environ.*, *44*(20), 2393–2400, doi:10.1016/j.atmosenv.2010.04.009.

Sheu, G.-R., and R. P. Mason (2001), An examination of methods for the measurements of reactive gaseous mercury in the atmosphere, *Environ. Sci. Technol.*, *35*(6), 1209–1216, doi:10.1021/es001183s.

Sigler, J. M., H. Mao, and R. Talbot (2009), Gaseous elemental and reactive mercury in Southern New Hampshire, *Atmos. Chem. Phys.*, *9*(6), 1929–1942, doi:10.5194/acp-9-1929-2009.

Slemr, F., E. G. Brunke, R. Ebinghaus, and J. Kuss (2011), Worldwide trend of atmospheric mercury since 1995, *Atmos. Chem. Phys.*, *11*(10), 4779–4787, doi:10.5194/acp-11-4779-2011.

Sommar, J., M. E. Andersson, and H. W. Jacobi (2010), Circumpolar measurements of speciated mercury, ozone and carbon monoxide in the boundary layer of the Arctic Ocean, *Atmos. Chem. Phys.*, *10*(11), 5031–5045, doi:10.5194/acp-10-5031-2010.

Song, S., et al. (2015), Top-down constraints on atmospheric mercury emissions and implications for global biogeochemical cycling, *Atmos. Chem. Phys. Discuss.*, *15*(4), 5269–5325, doi:10.5194/acpd-15-5269-2015.

Song, X., I. Cheng, and J. Lu (2009), Annual atmospheric mercury species in downtown Toronto, Canada, *J. Environ. Monit.*, *11*(3), 660–669, doi:10.1039/b815435j.

Streets, D. G., and S. T. Waldhoff (2000), Present and future emissions of air pollutants in China: SO_2, NO_x, and CO, *Atmos. Environ.*, *34*(3), 363–374, doi:10.1016/S1352-2310(99)00167-3.

Streets, D. G., J. M. Hao, Y. Wu, J. K. Jiang, M. Chan, H. Z. Tian, and X. B. Feng (2005), Anthropogenic mercury emissions in China, *Atmos. Environ.*, *39*(40), 7789–7806, doi:10.1016/j.atmosenv.2005.08.029.

United Nations Environment Programme (2013), Global mercury assessment 2013: Sources, emissions, releases and environmental transport, *Rep.*, UNEP Chemicals Branch Geneva, Switzerland.

Valente, R. J., C. Shea, K. L. Humes, and R. L. Tanner (2007), Atmospheric mercury in the Great Smoky Mountains compared to regional and global levels, *Atmos. Environ.*, *41*(9), 1861–1873, doi:10.1016/j.atmosenv.2006.10.054.

Wang, L., S. Wang, L. Zhang, Y. Wang, Y. Zhang, C. Nielsen, M. B. McElroy, and J. Hao (2014), Source apportionment of atmospheric mercury pollution in China using the GEOS-Chem model, *Environ. Pollut.*, *190*, 166–175, doi:10.1016/j.envpol.2014.03.011.

Wang, Y. Q., X. Y. Zhang, and R. R. Draxler (2009), TrajStat: GIS-based software that uses various trajectory statistical analysis methods to identify potential sources from long-term air pollution measurement data, *Environ. Modell. Software*, *24*(8), 938–939, doi:10.1016/j.envsoft.2009.01.004.

Wang, Z. W., Z. S. Chen, N. Duan, and X. S. Zhang (2007), Gaseous elemental mercury concentration in atmosphere at urban and remote sites in China, *J. Environ. Sci. China*, *19*(2), 176–180, doi:10.1016/S1001-0742(07)60028-X.

Wu, Y., S. Wang, D. G. Streets, J. Hao, M. Chan, and J. Jiang (2006), Trends in anthropogenic mercury emissions in China from 1995 to 2003, *Environ. Sci. Technol.*, *40*(17), 5312–5318, doi:10.1021/es060406x.

Ye, B. M., X. L. Ji, H. Z. Yang, X. H. Yao, C. K. Chan, S. H. Cadle, T. Chan, and P. A. Mulawa (2003), Concentration and chemical composition of $PM_{2.5}$ in Shanghai for a 1-year period, *Atmos. Environ.*, *37*(4), 499–510, doi:10.1016/S1352-2310(02)00918-4.

Zhang, H., X. W. Fu, C. J. Lin, X. Wang, and X. B. Feng (2015), Observation and analysis of speciated atmospheric mercury in Shangri-La, Tibetan Plateau, China, *Atmos. Chem. Phys.*, *15*(2), 653–665, doi:10.5194/acp-15-653-2015.

Zhu, J., et al. (2014), Characteristics of atmospheric mercury deposition and size-fractionated particulate mercury in urban Nanjing, China, *Atmos. Chem. Phys.*, *14*(5), 2233–2244, doi:10.5194/acp-14-2233-2014.